Original close-packed structure and magnetic properties of the $Pb_4Mn_9O_{20}$ manganite

Artem M. Abakumov [a,*], Joke Hadermann [a], Alexander A. Tsirlin [b,c], Haiyan Tan [a], Jo Verbeeck [a], Haitao Zhang [d], Evgeny V. Dikarev [d], Roman V. Shpanchenko [b], Evgeny V. Antipov [b]

[a] EMAT, University of Antwerp, Groenenborgerlaan 171, B-2020 Antwerp, Belgium
[b] Department of Chemistry, Moscow State University, 119992 Moscow, Russia
[c] Max Planck Institute for Chemical Physics of Solids, 01187 Dresden, Germany
[d] Department of Chemistry, University at Albany, SUNY, 1400 Washington Avenue CHM 315 Albany, NY 12222, USA

ABSTRACT

The crystal structure of the $Pb_4Mn_9O_{20}$ compound (previously known as "$Pb_{0.43}MnO_{2.18}$") was solved from powder X-ray diffraction, electron diffraction, and high resolution electron microscopy data (S.G. $Pnma$, $a = 13.8888(2)$ Å, $b = 11.2665(2)$ Å, $c = 9.9867(1)$ Å, $R_I = 0.016$, $R_P = 0.047$). The structure is based on a 6H $(cch)_2$ close packing of pure oxygen "h"-type (O_{16}) layers alternating with mixed "c"-type (Pb_4O_{12}) layers. The Mn atoms occupy octahedral interstices formed by the oxygen atoms of the close-packed layers. The MnO_6 octahedra share edges within the layers, whereas the octahedra in neighboring layers are linked through corner sharing. The relationship with the closely related $Pb_3Mn_7O_{15}$ structure is discussed. Magnetization measurements reveal a peculiar magnetic behavior with a phase transition at 52 K, a small net magnetization below the transition temperature, and a tendency towards spin freezing.

© 2009 Elsevier Inc. All rights reserved.

1. Introduction

Lead-containing transition metal oxides are currently the subject of intense research because of their peculiar crystal structure and unusual physical properties. The key feature of these compounds is the lone pair of the Pb^{+2} cation. The lone pair causes local structural distortions that strongly alter the crystal structures of transition metal oxides, e.g., the perovskite structure [1–4]. In some cases, polar distortions are observed, and piezo- or ferroelectric properties emerge. Yet, the presence of a transition metal cation results in magnetic interactions and magnetic ordering, leading to a possible coupling of electric polarization and magnetism. The latter point represents the main motivation for the recent studies of lead-containing transition metal oxides, although other unusual electronic phenomena have also been reported [5,6].

In the Pb–Mn–O system, several compounds have been isolated and structurally characterized. The Pb_2MnO_4 oxide contains infinite chains of edge-sharing MnO_6 octahedra and the Pb cations located between the chains [7]. The $Pb_3Mn_7O_{15}$ and $Pb_{1+x}Mn_8O_{16}$ compounds belong to the Mn-rich part of the phase diagram. $Pb_{1+x}Mn_8O_{16}$ is a tunnel manganite with a hollandite-type structure [8]. The structure of $Pb_3Mn_7O_{15}$ is based on a close-packed arrangement of pure oxygen and mixed Pb–O layers with the Mn cations located at the octahedral interstices between the layers [9–11]. Apart from these compounds, stable at ambient pressure, a few high pressure perovskite-related phases were observed: $PbMnO_3$ with a hexagonal 6H perovskite or nearly cubic 3C perovskite [12,13] and "$PbMnO_{2.75}$" having a structure obtained from perovskite by periodic fragmentation with parallel translational interfaces (crystallographic shear planes) [14].

Among these compounds, the "$Pb_{0.43}MnO_{2.18}$" composition was also reported as a single phase at ambient pressure, although neither unit cell parameters nor crystal structure were determined for this compound [15]. The material shows semiconducting behavior with activation energies $E_a = 0.12$ eV (140 K $< T < 300$ K) and 0.10 eV (300 K $< T < 500$ K) and room temperature conductivity $\sigma(300$ K$) = 0.13/\Omega$ cm. In the 300–750 K temperature range, the magnetic susceptibility follows the Curie–Weiss law with $\theta = -20$ K, indicating weak antiferromagnetic correlations.

In this contribution, we determine the true composition of the "$Pb_{0.43}MnO_{2.18}$" phase to be $Pb_4Mn_9O_{20}$ and solve the crystal structure of this mixed-valence Mn^{3+}/Mn^{4+} compound. We also investigate the low-temperature magnetic properties and compare the $Pb_4Mn_9O_{20}$ compound with the closely related $Pb_3Mn_7O_{15}$ manganite.

* Corresponding author. Fax: +32 3 2653257.
 E-mail address: artem.abakumov@ua.ac.be (A.M. Abakumov).

2. Experimental

2.1. Synthesis

The "$Pb_{0.43}MnO_{2.18}$" phase was obtained by thermal decomposition of the lead–manganese hexafluoroacetylacetonate $PbMn_2(hfac)_6$ at 600 °C for 72 h in air. The powder X-ray diffraction pattern of the material was very close to that of "$Pb_{0.43}MnO_{2.18}$" [15]. A primary electron diffraction (ED) investigation and analysis of chemical composition were performed, resulting in the unit cell parameters and the $Pb_4Mn_9O_{20}$ composition of this compound. After this, the $Pb_4Mn_9O_{20}$ sample was prepared using a conventional solid state reaction from a mixture of PbO (Aldrich) and Mn_2O_3 (Aldrich) with bulk $Pb_4Mn_9O_{17.5}$ composition. The initial oxides were intimately mixed in an agate mortar under acetone, pressed into a pellet and annealed at 750 °C for 20 h in air. After annealing, the sample was re-grinded, pressed into a pellet and annealed again at 750 °C for 20 h in O_2 flow. The sample was finally furnace-cooled in an O_2 atmosphere.

2.2. X-ray powder diffraction

X-ray powder diffraction (XRPD) patterns for phase analysis and Rietveld refinement were taken with a Philips X'pert diffractometer (Cu$K\alpha$ radiation, reflection mode). Structure determination was performed using the EXPO program [16,17]. The JANA2000 program package was used for the Rietveld refinement of the crystal structure [18].

2.3. Transmission electron microscopy

Samples for electron microscopy were prepared by crushing the powder sample in ethanol and depositing it on a holey carbon grid. Electron diffraction studies were performed using a Philips CM20 microscope. For high resolution transmission electron microscopy (HRTEM) a JEOL 4000EX microscope was used. Energy dispersive X-ray (EDX) spectra were obtained on the Philips CM20 microscope with an Oxford INCA system. The theoretical HRTEM images were calculated by means of the MacTempas software. Electron energy loss spectroscopy (EELS) data were acquired using a Gatan GIF200 system on a Philips CM30 microscope with an acceleration voltage of 300 kV and an energy resolution of 0.8 eV. All spectra were recorded in diffraction mode with a collection angle of 4.01 mrad and a convergence angle of 1.0 mrad. The EELSMODEL program [19,20] was used to extract the excitation edge fine structures from the recorded spectra.

2.4. Magnetic measurements

Magnetization measurements were done using the Quantum Design MPMS SQUID magnetometer in the temperature range 2–380 K in both field-cooled (FC) and zero-field-cooled (ZFC) regimes. Magnetization (M) vs. field (H) curves were measured in the field range 0–5 T after cooling the sample in zero field.

2.5. Electron localization function computation

The electron localization function (ELF) [21] was derived from the electronic density, as computed in a self-consistent band structure calculation. The spin-unpolarized calculations were done using the TB-LMTO-ASA code [22] in local density approximation (LDA). The Barth–Hedin exchange-correlation potential was employed [23], and a k mesh of 64 points was used. The LDA energy spectrum of $Pb_4Mn_9O_{20}$ is quite typical for the lead-containing transition metal compounds [3]. The Pb 6s states are

found at about –8 eV, the bands between −7 and −2 eV are formed by oxygen states, while the states near the Fermi level have a predominant manganese origin. The energy spectrum is gapless. However, this result is unlikely to be meaningful, because LDA is known to produce significant errors for the valence bands of the transition metal compounds due to the improper treatment of correlation effects in the localized d shell [6]. These errors are not crucial for the resulting ELF, since the function depends on the overall electronic density. Moreover, ELF is known to be rather insensitive to the accuracy of the band structure calculation and to the effects of spin polarization [21]. Therefore, the reported spin-unpolarized LDA calculations are sufficient for the identification of the lead lone pair. Yet a proper description of the valence bands is crucial for a discussion of the electronic properties, e.g., metallic or semiconducting behavior of $Pb_4Mn_9O_{20}$. To obtain reliable information on the electronic structure near the Fermi level and on the band gap, one has to account for electronic correlations and to perform more sophisticated calculations that lie beyond the scope of the present work.

3. Results and discussion

3.1. Lattice parameters and chemical composition

The approximate lattice parameters and space group of $Pb_4Mn_9O_{20}$ were determined using electron diffraction. The ED patterns of $Pb_4Mn_9O_{20}$ along the main zone axes (Fig. 1) can be indexed using a primitive orthorhombic unit cell with lattice parameters $a \approx 13.9$ Å, $b \approx 11.3$ Å, $c \approx 10.0$ Å. The reflection conditions derived from the ED patterns are $h\,k\,l$: no conditions, $0\,k\,l$: $k+l = 2n$, $h\,0\,l$: no conditions, $h\,k\,0$: $h = 2n$. The appearance of the $h\,0\,0$: $h \neq 2n$, $0\,k\,0$: $k \neq 2n$ and $0\,0\,l$: $l \neq 2n$ reflections on some ED patterns is due to the occurrence of double diffraction, as evidenced by their absence on the [100] pattern for the $0\,k\,0$ and $0\,0\,l$ reflections, and on the [001] pattern for the $h\,0\,0$ reflections. These reflection conditions correspond to the extinction symbol Pn_a, with two possible space groups $Pn2_1a$ and $Pnma$. The most symmetric $Pnma$ space group was taken for structure solution.

The XRPD pattern of the $Pb_4Mn_9O_{20}$ phase demonstrates close resemblance to the XRPD pattern of the "$Pb_{0.43}MnO_{2.18}$" phase [15], indicating that both compounds are identical. The lattice parameters determined from the electron diffraction data allow the complete indexation of the XRPD pattern. The refined values of the lattice parameters are $a = 13.8888(2)$ Å, $b = 11.2665(2)$ Å, $c = 9.9867(1)$ Å. The $0\,k\,l$, $k+l = 2n$, $h\,k\,0$, $h = 2n$ reflection conditions,

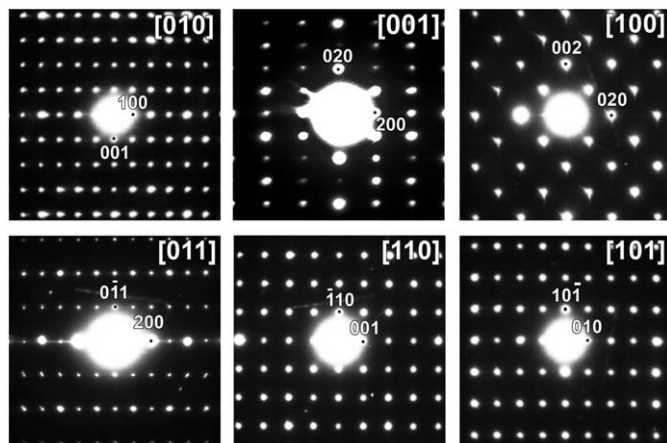**Fig. 1.** Electron diffraction patterns for $Pb_4Mn_9O_{20}$.

observed in the XRPD pattern, are in agreement with the space group *Pnma*.

The $Pb_4Mn_9O_{20}$ composition, derived from the results of the Rietveld refinement, was confirmed by EDX, EELS and elemental analyses (wt%, calculated for $Pb_4Mn_9O_{20}$: Pb 50.44, Mn 30.09, O 19.47; found: Pb 50.9, Mn 29.9, O 19.5, performed by Maxima Laboratories Inc., Ontario, Canada). Fifteen EDX spectra taken from 10 different crystallites revealed a Pb:Mn ratio of 32(1):68(1), which is in good agreement with the nominal Pb:Mn ratio of 30.8:69.2. The valence of manganese (V_{Mn}) was derived from the EELS spectra, which can be used to determine the valency of ionic materials in several ways [24–27]. One method that was shown to give superior results is to measure the distance in energy onset between the oxygen K edge and the transition metal $L_{2,3}$ edge of oxides as was shown for niobium oxides by Bach et al. [28]. Recently we reported a linear dependence of the Mn valence on the measured energy distances (ΔE) between the oxygen K edge and the manganese $L_{2,3}$ edge as follows:

$$\Delta E = a + b * V_{Mn}$$

with $a = 104.108 \pm 0.195\,eV$ and $b = 2.238 \pm 0.063\,eV$ [29]. We adopt this method here and use the same experimental condition and data analysis to determine the Mn valence. From the analysis of about 200 spectra it was found that the edge onset difference of oxygen K and manganese $L_{2,3}$ edges of $Pb_4Mn_9O_{20}$ is 111.89(6) eV (Fig. 2). From the above formula, the Mn valence was calculated as $V_{Mn} = +3.48(3)$. It correlates well with the $V_{Mn} = +3.55$ obtained for the nominal composition. The slightly smaller measured V_{Mn} can be attributed to the presence of oxygen vacancies, according to a $Pb_4Mn_9O_{19.66}$ composition.

3.2. Structure solution

Direct methods based on integrated intensities extracted with a Le Bail fit were applied to the structure solution that resulted in the atomic coordinates of the Pb atoms. The coordinates of the Mn and O atoms were found using difference Fourier maps. In order to reduce correlations, the atomic positions were grouped according to their chemical type and refined with a common atomic displacement parameter (ADP) for each group. The refinement converged smoothly and revealed an excellent agreement

between the experimental and calculated XRPD profiles ($R_I = 0.016$, $R_P = 0.047$). In order to check the possible presence of oxygen vacancies, the occupancy factors of the oxygen positions were refined. For all sites, except O(2), O(7), and O(12), the occupancy factors were very close to unity. The refined occupancy factors for the O(2), O(7), and O(12) positions are $g(O(2)) = 0.94(2)$, $g(O(7)) = 0.96(2)$, $g(O(12)) = 0.94(2)$, corresponding to a $Pb_4Mn_9O_{19.68}$ composition, in good agreement with $V_{Mn} = +3.48$ found by the EELS analysis. However, one should note that the refinement of the occupancies of the oxygen positions did not lead to any improvement of the fit or to a decrease of the reliability factors. It should be taken into account that a refinement of the occupancies of oxygen positions in the presence of heavy scatterers (such as Pb) cannot be done accurately using XRPD data. Thus, the final refinement was performed with full occupancies, leaving the question of the exact amount and location of the oxygen vacancies for a neutron diffraction experiment. The crystallographic data and atomic coordinates of $Pb_4Mn_9O_{20}$ are summarized in Tables 1 and 2. The relevant interatomic distances are listed in Table 3. Experimental, calculated, and difference XRPD profiles are shown in Fig. 3.

The crystal structure was confirmed by high resolution transmission electron microscopy. A representative HRTEM image is shown in Fig. 4. A calculated image using the structural data from Table 2 is also shown, outlined by a white border on the experimental image. The image is calculated at a focus value

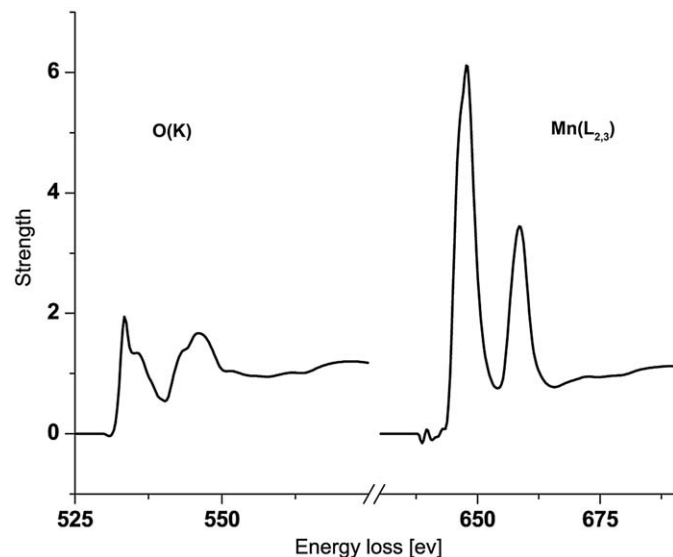**Fig. 2.** The excitation edge fine structures of oxygen K-edge and manganese $L_{2,3}$-edge from $Pb_4Mn_9O_{20}$ after deconvolution of multiple scattering and background subtraction.

Table 1
Selected parameters from Rietveld refinement for $Pb_4Mn_9O_{20}$.

Formula	$Pb_4Mn_9O_{20}$
Space group	*Pnma*
a (Å)	13.8888(2)
b (Å)	11.2665(2)
c (Å)	9.9867(1)
Z	4
Cell volume (Å^3)	1562.70(5)
Calculated density (g/cm^3)	6.982
Radiation	$CuK\alpha$, $\lambda = 1.54184$ Å
2θ range, step (deg)	$5 \leq 2\theta \leq 110$, 0.02
Parameters refined	56
R_I, R_P, R_{wP}	0.016, 0.047, 0.063

Table 2
Positional and atomic displacement parameters for $Pb_4Mn_9O_{20}$.

Atom	Position	x/a	y/b	z/c	U_{iso} (Å^2)
Pb(1)	4c	0.9391(1)	1/4	0.7132(2)	0.0212(3)
Pb(2)	4c	0.1074(1)	3/4	0.9221(2)	0.0212(3)
Pb(3)	8d	0.07627(8)	0.9329(1)	0.6400(1)	0.0212(3)
Mn(1)	4c	0.3274(5)	3/4	0.1647(6)	0.0132(6)
Mn(2)	8d	0.8211(3)	0.6204(4)	0.0870(4)	0.0132(6)
Mn(3)	8d	0.6631(3)	0.3838(4)	0.0825(4)	0.0132(6)
Mn(4)	4c	0.6682(4)	1/4	0.3304(6)	0.0132(6)
Mn(5)	8d	0.1716(3)	0.5093(4)	0.1730(4)	0.0132(6)
Mn(6)	4a	0	0	0	0.0132(6)
O(1)	8d	0.097(1)	0.374(1)	0.082(1)	0.016(1)
O(2)	8d	0.083(1)	0.0620(1)	0.106(1)	0.016(1)
O(3)	8d	0.9119(9)	0.505(1)	0.147(1)	0.016(1)
O(4)	4c	0.597(1)	1/4	0.173(2)	0.016(1)
O(5)	8d	0.5932(9)	0.506(1)	0.162(1)	0.016(1)
O(6)	4c	0.396(1)	3/4	0.325(2)	0.016(1)
O(7)	8d	0.909(1)	0.638(1)	0.424(1)	0.016(1)
O(8)	4c	0.265(1)	3/4	0.003(2)	0.016(1)
O(9)	4c	0.242(1)	1/4	0.004(2)	0.016(1)
O(10)	8d	0.752(1)	0.868(1)	0.242(1)	0.016(1)
O(11)	8d	0.247(1)	0.495(1)	0.004(1)	0.016(1)
O(12)	8d	0.235(1)	0.377(1)	0.255(1)	0.016(1)

of $f = -350\,\text{Å}$ and a thickness $t = 30\,\text{Å}$, and shows excellent agreement with the experimental one. On this simulation, the dark areas correspond to the projection of the lead atom columns, and the bright areas to the projection of the oxygen columns.

3.3. Structure discussion

The crystal structure of $Pb_4Mn_9O_{20}$ is shown in Fig. 5a. From the [010] projection (Fig. 5b), it becomes clear that the structure

Table 3
Selected interatomic distances for $Pb_4Mn_9O_{20}$.

Pb(1)–O(2)	2.343(13) × 2	Mn(3)–O(4)	1.980(13) × 1
Pb(1)–O(5)	2.828(13) × 2	Mn(3)–O(5)	1.864(14) × 1
Pb(1)–O(6)	2.555(19) × 1	Mn(3)–O(7)	1.884(14) × 1
Pb(1)–O(7)	2.819(14) × 2	Mn(3)–O(8)	1.998(14) × 1
Pb(1)–O(10)	2.981(14) × 2	Mn(3)–O(11)	2.035(14) × 1
		Mn(3)–O(12)	1.906(16) × 1
Pb(2)–O(2)	2.372(13) × 2	BVS = 3.84	
Pb(2)–O(3)	2.965(13) × 2	$\Delta d = 6.3 \times 10^{-3}$	
Pb(2)–O(8)	2.334(19) × 1		
		Mn(4)–O(1)	1.920(15) × 2
Pb(3)–O(3)	2.284(13) × 1	Mn(4)–O(4)	1.86(2) × 1
Pb(3)–O(5)	2.504(13) × 1	Mn(4)–O(9)	1.95(2) × 1
Pb(3)–O(7)	2.402(13) × 1	Mn(4)–O(12)	1.904(16) × 2
Pb(3)–O(11)	2.887(14) × 1	BVS = 3.94	
Pb(3)–O(12)	2.933(14) × 1	$\Delta d = 1.2 \times 10^{-3}$	
Mn(1)–O(6)	1.86(2) × 1	Mn(5)–O(1)	2.059(14) × 1
Mn(1)–O(7)	1.920(14) × 2	Mn(5)–O(2)	1.879(14) × 1
Mn(1)–O(8)	1.83(2) × 1	Mn(5)–O(5)	1.978(14) × 1
Mn(1)–O(10)	1.928(16) × 2	Mn(5)–O(10)	1.969(15) × 1
BVS = 4.08		Mn(5)–O(11)	1.997(15) × 1
$\Delta d = 2.5 \times 10^{-3}$		Mn(5)–O(12)	1.913(16) × 1
		BVS = 3.42	
Mn(2)–O(1)	2.033(14) × 1	$\Delta d = 5.2 \times 10^{-3}$	
Mn(2)–O(3)	1.909(14) × 1		
Mn(2)–O(6)	1.992(14) × 1	Mn(6)–O(1)	2.124(14) × 2
Mn(2)–O(9)	1.932(14) × 1	Mn(6)–O(2)	2.069(13) × 2
Mn(2)–O(10)	1.831(15) × 1	Mn(6)–O(3)	1.911(13) × 2
Mn(2)–O(11)	1.852(14) × 1	BVS = 2.95	
BVS = 3.84		$\Delta d = 11.8 \times 10^{-3}$	
$\Delta d = 8.3 \times 10^{-3}$			

is based on a 6H $(cch)_2$ sequence of close-packed layers formed either by oxygen atoms or by the Pb and O atoms together and alternating along the a axis. The Mn atoms occupy octahedral interstices between the close-packed layers (Figs. 5b, c). Only those interstices formed exclusively by oxygen atoms are occupied.

The structure of the mixed Pb–O layers can be derived from the structure of a conventional oxygen close-packed layer by a replacement of groups of four neighboring oxygen atoms with four Pb atoms (see Fig. 6a), so that the layer acquires the (Pb_4O_{12}) composition. These layers are always of the "c"-type, whereas pure oxygen (O_{16}) layers (Fig. 6b) are of the "h"-type. Thus the layer sequence can be written as $(Pb_4O_{12})_c$–$(Pb_4O_{12})_c$–$(O_{16})_h$–$(Pb_4O_{12})_c$–$(Pb_4O_{12})_c$–$(O_{16})_h$. Four Pb atoms in the (Pb_4O_{12}) layers form rhombus-like groups. Due to displacement of the Pb atoms from their ideal positions in the close-packed layers, these

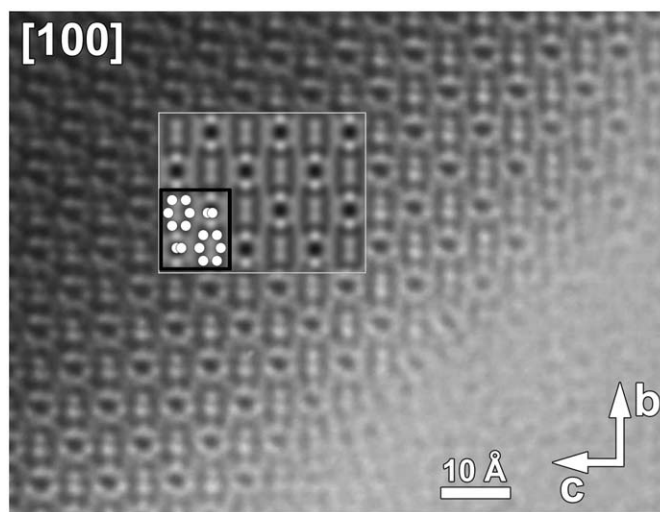**Fig. 4.** Experimental and calculated (in white border) HRTEM image of $Pb_4Mn_9O_{20}$. The size of one unit cell is indicated on the simulation by a black rectangle. White dots indicate the positions of the Pb columns.
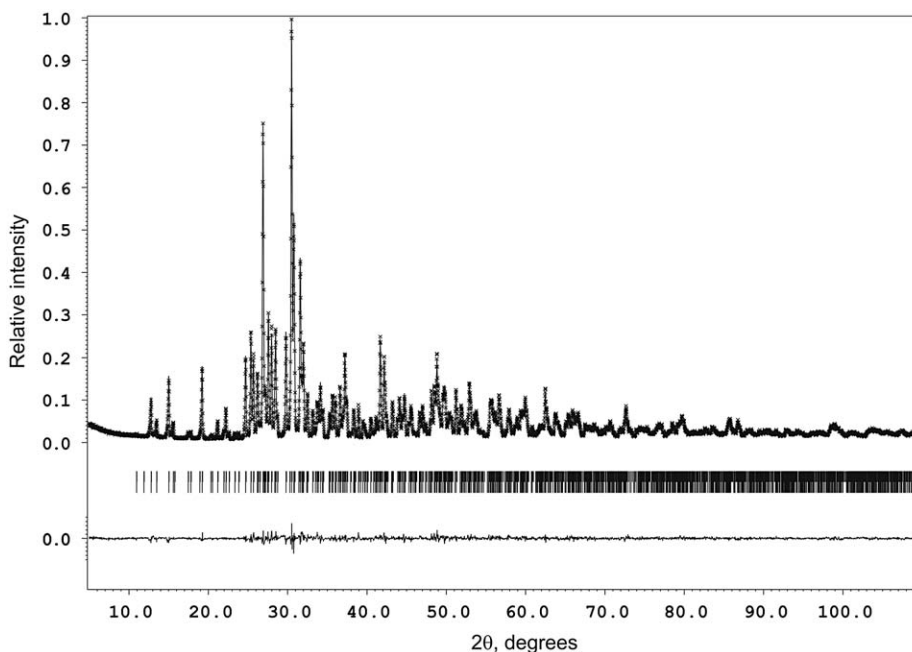

Fig. 3. Experimental, calculated and difference XRPD pattens for $Pb_4Mn_9O_{20}$.

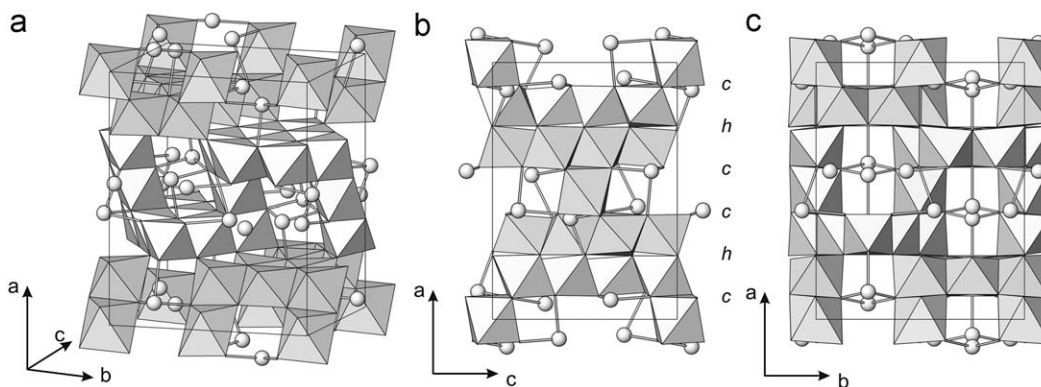**Fig. 5.** The crystal structure of $Pb_4Mn_9O_{20}$: (a) 3D view; (b) [010] projection; (c) [001] projection. The Pb atoms are shown as spheres; the Mn atoms are situated inside the octahedra. The sequence of close-packed layers is shown.
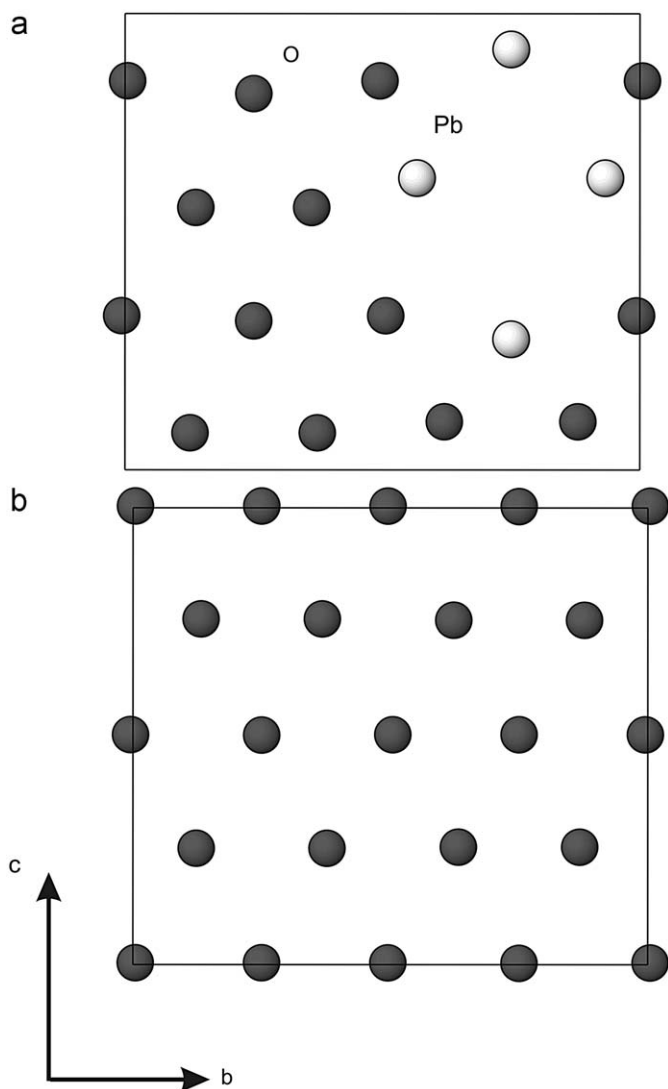

Fig. 6. The structure of the (Pb_4O_{12}) (a) and (O_{16}) (b) close-packed layers.

Fig. 7. Filling of the octahedral interstices located between the (Pb_4O_{12}) and (O_{16}) layers (a) and between the adjacent (Pb_4O_{12}) layers (b). The Pb atoms are shown as spheres; the Mn atoms are situated inside the octahedra. Part (a) also shows ELF isosurface for $\eta = 0.75$.

rhombi have a longer diagonal aligned along the c axis. The rhombi form a quasi-1D sequence along the c axis, breaking the close-packed layers into oxygen and lead bands, alternating along the b axis. The bands of the Pb rhombi in the two adjacent (Pb_4O_{12}) layers are displaced with respect to each other by $1/4b$; this severely restricts the amount of octahedral interstices

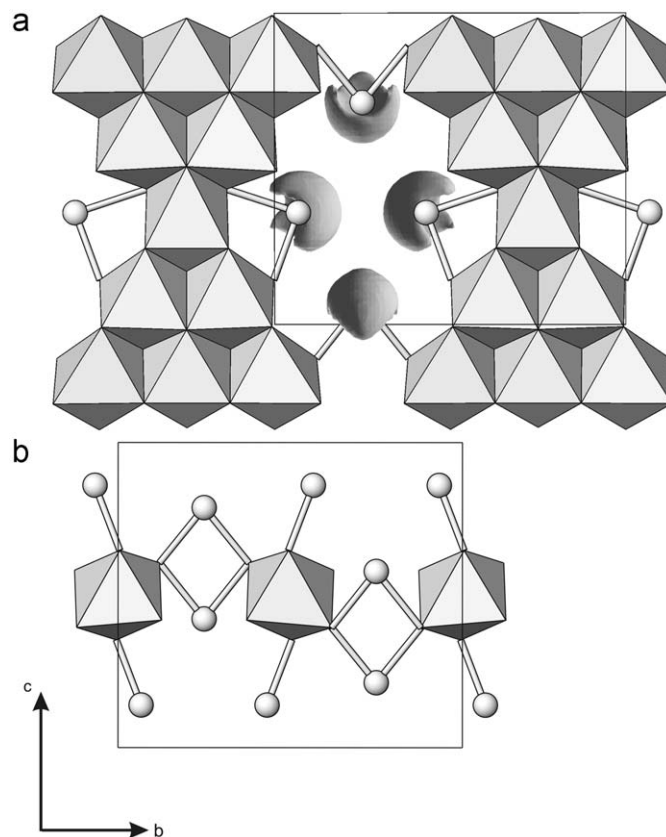available for the Mn atoms between these layers. There are eight MnO_6 octahedra between the (Pb_4O_{12}) and (O_{16}) layers (Fig. 7a), and two MnO_6 octahedra per unit cell between the adjacent (Pb_4O_{12}) layers (Fig. 7b), resulting in a $Mn_8-(Pb_4O_{12})_c-Mn_2-(Pb_4O_{12})_c-Mn_8-(O_{16})_h-Mn_8-(Pb_4O_{12})_c-Mn_2-(Pb_4O_{12})_c-Mn_8-(O_{16})_h = Pb_{16}Mn_{36}O_{80} = 4 \times Pb_4Mn_9O_{20}$ composition. The MnO_6 octahedra between the (Pb_4O_{12}) and (O_{16}) layers are combined by edge sharing into quasi-1D tapes. The MnO_6 octahedra in neighboring layers are connected exclusively by corner sharing. The latter is typical for "c"-type close-packed layers, whereas face-sharing could be expected for the "h"-type layers. However, the face-sharing arrangement is not realized in the $Pb_4Mn_9O_{20}$

structure due to a mutual displacement of the (Pb_4O_{12}) layers above and below the "h"-type (O_{16}) layer that makes only one of two face-sharing octahedral interstices available for the Mn atoms.

The octahedral oxygen environment of the Mn atoms demonstrate different degrees of distortion, which can be evaluated using an octahedral distortion parameter Δd [30]:

$$\Delta d = \left(\frac{1}{6}\right) \sum_{n=1-6} [(d_n - d)/d]^2$$

where d_n is the individual Mn–O distances and d is the average $\langle Mn-O \rangle$ distance (see Table 3). The weakest distortion ($\Delta d = 1.2–2.5 \times 10^{-3}$) is observed for the Mn(1) and Mn(4) atoms. At the same time, the bond valence sum (BVS) for these atoms are very close to 4. The Mn(6)O_6 octahedron demonstrates the largest distortion ($\Delta d = 11.8 \times 10^{-3}$) with two long Mn(6)–O(1) distances of 2.12 Å, two short Mn(6)–O(3) distances of 1.91 Å and two intermediate Mn(6)–O(2) distances of 2.07 Å. Such a coordination is typical for the Mn^{+3} cations with an intrinsic Jahn–Teller distortion. Indeed, the BVS for the Mn(6) cation is close to 3. The Mn(2), Mn(3), and Mn(5) sites show an intermediate degree of octahedral distortion, as well as BVS values between 3 and 4. The geometry of the octahedral coordination of the Mn atoms indicates that at least partial charge ordering can take place; this could be expected keeping in mind the formal Mn valence close to +3.5.

The coordination environment of the Pb atoms is virtually identical for all three positions and consists of three short Pb–O distances with two oxygen atoms from the same (Pb_4O_{12}) layer and with one oxygen atom from the neighboring (O_{16}) layer. Such coordination environment is typical for Pb^{2+} cations and can be found, for example, in the room temperature form of Pb_3O_4 [31], several Pb_2MO_4 oxides ($M = Mn^{4+}$, Sn^{4+}, Pt^{4+}) [7,32,33], and the $(Sb_{1-x}Pb_x)_2(Mn_{1-y}Sb_y)O_4$ solid solutions [34]. The three-fold coordination environment is completed to a tetrahedron by a localized $6s^2$ lone electron pair of Pb^{+2}. The localization of the lone pairs is evident from the ELF plot in Fig. 7a. The lone pairs of the neighboring lead atoms "condense" and form non-bonding regions within the structure, similar to other Pb^{+2}-containing oxides [7,31,34].

The $Pb_4Mn_9O_{20}$ structure is closely related to the structure of the $Pb_3M_7O_{15}$ ($M = Mn$, Rh) compounds [9,10,35]. This is also based on a close-packed arrangement of pure oxygen and mixed Pb–O layers. The $Pb_3M_7O_{15}$ structures can be derived from the 2H (hh) close packing by replacing every third (O_{12}) layer with the (Pb_6O_6) layer. In both $Pb_4Mn_9O_{20}$ and $Pb_3M_7O_{15}$ structures, the M atoms occupy the octahedral interstices formed exclusively by oxygen atoms. The remaining oxygen atoms in the (Pb_6O_6) layers form a common triangular face of two face-sharing MnO_6 octahedra, so that in $Pb_3M_7O_{15}$ such octahedra share common vertices, edges, and faces, whereas in $Pb_4Mn_9O_{20}$ the face-sharing arrangement is absent.

3.4. Magnetic properties

The magnetic susceptibility of $Pb_4Mn_9O_{20}$ was measured in different applied fields. A number of representative curves are shown in Fig. 8. Above 80 K, $Pb_4Mn_9O_{20}$ reveals paramagnetic behavior. The susceptibility follows the Curie–Weiss law $\chi = \chi_0 + C/(T-\theta)$ with a Curie constant $C = 1.796(5)$ emu K/(mol Mn), a Weiss temperature $\theta = 37.7(2)$ K, and a temperature-independent contribution $\chi_0 = -1.4(2) \times 10^{-4}$ emu/mol. The Curie constant corresponds to an effective moment $\mu_{eff} = 3.79\,\mu_B$ per Mn atom, while the positive Weiss temperature implies predominant ferromagnetic interactions. The effective moment is roughly equal to the expected spin-only value for Mn^{+4} ($S = 3/2$,
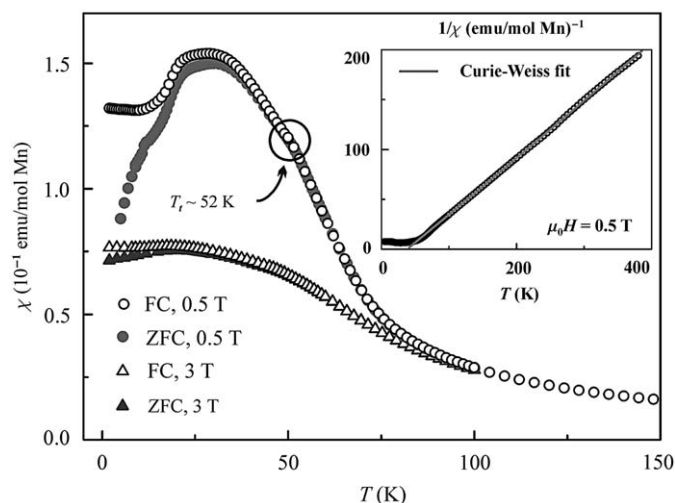

Fig. 8. Temperature dependence of the magnetic susceptibility measured in the applied field $\mu_0H = 0.5$ and 3 T in both field-cooled (FC) and zero-field-cooled (ZFC) regimes. The inset shows the inverse susceptibility and the fit with the Curie–Weiss law.

$\mu_{eff} = 3.87\,\mu_B$), while the combination of Mn^{+3} and Mn^{+4} with an average oxidation state of +3.5 should lead to a higher μ_{eff} of $4.42\,\mu_B$. The underestimate of the effective moment can indicate an incomplete electronic localization in $Pb_4Mn_9O_{20}$, although other reasons (e.g., spin–orbit coupling) may be relevant as well. The positive Weiss temperature contrasts with the negative value of $\theta = -20$ K, reported by Latourette et al. [15]. This discrepancy may be explained by the different sample composition (Latourette et al. [15] considered $Pb_4Mn_2O_{20}$ to be an oxidized form of $Pb_3Mn_7O_{15}$, although the Pb:Mn ratio is in fact different) or by the different temperature range used for the fitting.

Below 80 K, the low-field susceptibility (collected at $\mu_0H = 0.5$ T) shows a positive deviation from the Curie–Weiss law, indicating the onset of ferromagnetic correlations. There is a kink at $T_t \sim 52$ K, where the slope of the curve is changed, and a slight divergence of the field-cooled and zero-field-cooled curves appears. This kink is not related to the change of the step in the data collection, because the kink is seen both in the FC and ZFC data. The latter (filled circles in Fig. 8) were collected with the constant step of 0.6 K in the temperature range from 45 to 60 K. The divergence also appears at higher fields ($\mu_0H = 3$ T), although the kink is suppressed, and the susceptibility values get smaller, as compared to the low-field measurements. Below T_t, there is a further increase of the susceptibility. If the applied field is high ($\mu_0H = 3$ T), the low-temperature behavior is rather simple: the FC susceptibility becomes temperature-independent below 25 K, while the ZFC one slightly decreases. This corresponds to the regular spin-glass behavior. However, the low-field measurements reveal more complex features. Both the FC and ZFC curves show a maximum at 25–30 K and a sharp drop of the susceptibility below the maximum along with the enhanced divergence of the two curves. Additionally, there is a clear anomaly in the ZFC curve at 11–12 K.

Field dependence of the magnetization follows the basic features of the susceptibility data. The M vs. H curves become non-linear below 80 K, while the curves measured below T_t show a hysteresis (Fig. 9). The hysteresis is hardly seen at 40 K, but at lower temperatures it appears more pronounced and points to the formation of an uncompensated magnetic moment. The value of the saturation magnetization (M_s) is rather small and amounts to about $0.5\,\mu_B$ per Mn atom.

The phenomenological interpretation of the magnetization data is rather straight-forward. $Pb_4Mn_9O_{20}$ reveals ferromagnetic correlations that manifest themselves below 80 K and fit the
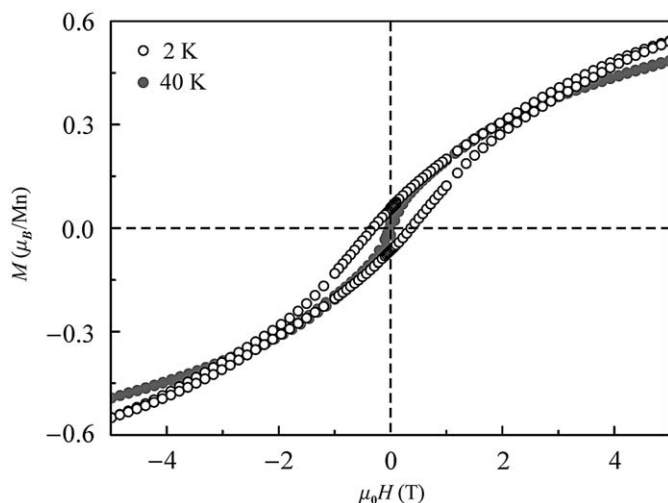
Fig. 9. Magnetization curves collected at 2 and 40 K.

positive Weiss temperature. The anomaly at $T_t \sim 52$ K likely corresponds to the onset of the long-range ordering. However, this ordering is not entirely ferromagnetic, because M_s is well below the expected values of $3\,\mu_B$ for Mn^{+4} ($S = 3/2$) or $4\,\mu_B$ for Mn^{+3} ($S = 2$). The small net magnetization of antiferromagnets is usually caused by a spin canting due to Dzyaloshinsky–Moriya interactions (for example, $LaMn_7O_{12}$ shows canted antiferromagnetic ordering with M_s of about $0.3\,\mu_B$ [36]). Still, the saturation magnetization of $Pb_4Mn_9O_{20}$ is rather high and may also indicate a ferrimagnetic ground state. Note that the antiferromagnetic interactions and ferrimagnetic or canted antiferromagnetic ordering do not contradict the positive Weiss temperature, because the latter is a linear combination of all the exchange couplings in the system under investigation. Antiferromagnetic interactions may lead to an antiferromagnetic ground state even in the case when ferromagnetic interactions dominate.

The low-temperature magnetic behavior of $Pb_4Mn_9O_{20}$ is more difficult to understand. The divergence of the FC and ZFC curves usually implies the formation of a spin glass. Thus, there is a tendency towards spin freezing at low temperatures, although the system does not behave as a regular spin glass, and the clear magnetization hysteresis is observed even at 2 K (see Fig. 9). Moreover, the low-field data reveal additional transitions (or, at least, changes) at 10–25 K. These changes may be associated with spin reorientation, as it was recently suggested for $Pb_3Mn_7O_{15}$ [10].

Unfortunately, a microscopic interpretation of the observed magnetic properties seems hardly possible. The crystal structure of $Pb_4Mn_9O_{20}$ is complex, while the mixed-valence state of manganese suggests the presence of charge degrees of freedom along with spin and orbital effects. From a very general point of view, the interplay of ferromagnetic and antiferromagnetic interactions in $Pb_4Mn_9O_{20}$ is not surprising due to the numerous inequivalent exchange pathways and the possibility of a double exchange. These features usually lead to intrinsic frustration and to spin-glass behavior (or at least partial spin freezing) of mixed-valence manganites. Similar behavior is observed in $Pb_4Mn_9O_{20}$ and looks natural, although the low-temperature details remain unclear. Further understanding of the magnetic properties requires a careful low-temperature structural study and the identification of the valence states for individual manganese positions.

The obtained experimental data point to both similarities and differences in the magnetic behavior of $Pb_4Mn_9O_{20}$ and $Pb_3Mn_7O_{15}$. These two compounds have related crystal structures and similar mixed-valence state of manganese (at least, with

respect to the average oxidation state). Both materials show a net magnetization at low temperatures, although the values of uncompensated moment are somewhat different (0.5 and $0.13\,\mu_B$ for $Pb_4Mn_9O_{20}$ and $Pb_3Mn_7O_{15}$ [10], respectively). Moreover, the overall energy scale for exchange interactions is also different. In the case of $Pb_3Mn_7O_{15}$, $\theta = -520$ K, while the Weiss temperature of $Pb_4Mn_9O_{20}$ amounts to 38 K and has the opposite sign. Thus, the structural changes associated with variation in the Pb:Mn ratio bear strong influence on the magnetic properties. Both compounds show intricate (and somewhat similar) low-temperature behavior that requires further structural and physical studies.

4. Conclusions

The $Pb_4Mn_9O_{20}$ compound, known earlier as "$Pb_{0.43}MnO_{2.18}$", was synthesized by thermal decomposition of heterometallic lead–manganese β-diketonate and by solid state reaction. Its structure is based on a 6H $(cch)_2$ close packing of the "h"-type (O_{16}) layers alternating with the "c"-type (Pb_4O_{12}) layers. The Mn atoms are located at the octahedral interstices formed by the oxygen atoms of the close-packed layers resulting in a Mn_8–$(Pb_4O_{12})_c$–Mn_2–$(Pb_4O_{12})_c$–Mn_8–$(O_{16})_h$–Mn_8–$(Pb_4O_{12})_c$–Mn_2–$(Pb_4O_{12})_c$–Mn_8–$(O_{16})_h$ layer sequence. The MnO_6 octahedra share edges within the layers, whereas the octahedra in neighboring layers are linked through corner sharing. The analysis of the octahedral distortion reveals partial ordering of the Mn^{+3} and Mn^{+4} cations. The $Pb_4Mn_9O_{20}$ structure is closely related to the structure of $Pb_3Mn_7O_{15}$, which is based on a 2H (hh) close packing with an alternation of two (O_{12}) layer and one (Pb_6O_6) layer. $Pb_4Mn_9O_{20}$ demonstrates paramagnetic behavior down to $T = 52$ K and a complex magnetic behavior below the transition temperature with a tendency to a spin-glass-like state.

Appendix A. Supplementary material

Supplementary data associated with this article can be found in the online version at doi:10.1016/j.jssc.2009.06.003.

References

[1] A.M. Abakumov, J. Hadermann, S. Bals, I.V. Nikolaev, E.V. Antipov, G. Van Tendeloo, Angew. Chem. Int. Ed. 45 (2006) 6697–6700.
[2] A. Arévalo-López, M.Á. Alario-Franco, J. Solid State Chem. 180 (2007) 3271–3279.
[3] R.V. Shpanchenko, V.V. Chernaya, A.A. Tsirlin, P.S. Chizhov, D.E. Sklovsky, E.V. Antipov, E.P. Khlybov, V. Pomjakushin, A.M. Balagurov, J.E. Medvedeva, E.E. Kaul, C. Geibel, Chem. Mater. 16 (2004) 3267–3273.
[4] A.A. Belik, M. Azuma, T. Saito, Y. Shimakawa, M. Takano, Chem. Mater. 17 (2005) 269–273.
[5] T. Waki, Y. Morimoto, C. Michioka, M. Kato, H. Kageyama, K. Yoshimura, S. Nakatsuji, O. Sakai, Y. Maeno, H. Mitamura, T. Goto, J. Phys. Soc. Jpn. 73 (2004) 3435–3438.

[6] A.A. Tsirlin, A.A. Belik, R.V. Shpanchenko, E.V. Antipov, E. Takajama-Muromachi, H. Rosner, Phys. Rev. B 77 (2008) 092402.

[7] A. Teichert, H.k. Müller-Buschbaum, Z. Anorg. Allg. Chem. 598 (1991) 319–325.

[8] J.E. Post, D.L. Bish, Am. Miner. 74 (1989) 913–917.

[9] Y. Le Page, L.D. Calvert, Acta Cryst. C 40 (1984) 1787–1789.

[10] N.V. Volkov, K.A. Sablina, O.A. Bayukov, E.V. Eremin, G.A. Petrakovskii, D.A. Velikanov, A.D. Balaev, A.F. Bovina, P. Böni, E. Clementyev, J. Phys. Condens. Matter 20 (2008) 055217.

[11] J.C.E. Rasch, D.V. Sheptyakov, J. Schefer, L. Keller, M. Boehm, F. Gozzo, N.V. Volkov, K.A. Sablina, G.A. Petrakovskii, H. Grimmer, K. Conder, J.F. Löffler, J. Solid State Chem., doi:10.1016/j.jssc.2009.02.001.

[12] C. Bougerol, M.F. Gorius, P. Bordet, I.E. Grey, Acta. Cryst. A 58 (2002) C23.

[13] K. Oka, M. Azuma, S. Hirai, A.A. Belik, H. Kojitani, M. Akaogi, M. Takano, Y. Shimakawa, Inorg. Chem. 48 (2009) 2285–2288.

[14] C. Bougerol, M.F. Gorius, I.E. Grey, J. Solid State Chem. 169 (2002) 131–138.

[15] B. Latourette, M. Devalette, F. Guillen, C. Fouassier, Mat. Res. Bull. 13 (1978) 567–574.

[16] A. Altomare, M.C. Burla, G. Cascarano, C. Giacovazzo, A. Guagliardi, A.G.G. Moliterni, G. Polidori, J. Appl. Cryst. 28 (1995) 842–846.

[17] A. Altomare, G. Cascarano, C. Giacovazzo, A. Guagliardi, M.C. Burla, G. Polidori, M.J. Camalli, Appl. Cryst. 27 (1994) 435–436.

[18] V. Petricek, M. Dusek, The Crystallographic Computing System JANA2000, Institute of Physics, Praha, Czech Republic, 2000.

[19] G. Bertoni, J. Verbeeck, Ultramicroscopy 108 (2008) 782–790.

[20] J. Verbeeck, S. Van Aert, Ultramicroscopy 101 (2004) 207–224.

[21] A. Savin, R. Nesper, S. Wengert, T.F. Fässler, Angew. Chem. Int. Ed. 36 (1997) 1808–1832.

[22] G. Krier, O. Jepsen, A. Burkhart, O.K. Andersen, The TB-LMTO-ASA Program, Stuttgart, 1995.

[23] U. von Barth, L. Hedin, J. Phys. C 5 (1972) 1629–1642.

[24] H. Kurata, C. Colliex, Phys. Rev. B 48 (1993) 2102–2108.

[25] J.H. Rask, B.A. Miner, P.R. Buseck, Ultramicroscopy 21 (1987) 321–326.

[26] T. Riedl, T. Gemming, K. Wetzig, Ultramicroscopy 106 (2006) 284–291.

[27] T. Riedl, T. Gemming, W. Gruner, J. Acker, K. Wetzig, Micron 38 (2007) 224–230.

[28] D. Bach, H. Stormer, R. Schneider, D. Gerthsen, J. Verbeeck, Microsc. Microanalysis 12 (2006) 416–423.

[29] H. D'Hondt, J. Hadermann, A.M. Abakumov, A.S. Kalyuzhnaya, M.G. Rozova, A.A. Tsirlin, R. Nath, H. Tan, J. Verbeeck, E.V. Antipov, G. Van Tendeloo, J. Solid State Chem. 182 (2009) 356–363.

[30] J.A. Alonso, M.J. Martinez-Lopez, M.T. Casais, M.T. Fernandez-Diaz, Inorg. Chem. 39 (2000) 917–923.

[31] J.R. Gavarri, D. Weigel, Phase Transitions 38 (1992) 127–220.

[32] J.R. Gavarri, J.P. Vigouroux, G. Calvarin, A.W. Hewat, J. Solid State Chem. 36 (1981) 81–90.

[33] N. Bettahar, P. Conflant, F. Abraham, D. Thomas, J. Solid State Chem. 67 (1987) 85–90.

[34] A.M. Abakumov, M.G. Rozova, E.V. Antipov, J. Hadermann, G. Van Tendeloo, M.V. Lobanov, M. Greenblatt, M. Croft, E.V. Tsiper, A. Llobet, K.A. Lokshin, Y. Zhao, Chem. Mater. 17 (2005) 1123–1134.

[35] J. Omaly, R. Kohlmuller, P. Batail, R. Chevalier, Acta Cryst. B 36 (1980) 1040–1044.

[36] A. Prodi, E. Gilioli, R. Cabassi, F. Bolzoni, F. Licci, Q. Huang, J.W. Lynn, M. Affronte, A. Gauzzi, M. Marezio, Phys. Rev. B 79 (2009) 085105.